Diffusion driven barite front nucleation and crystallisation in sedimentary rocks

Bruno Leclere, Hannelore Derluyn, Eric Gaucher, Sylvain Calassou, Joseph Diaz, Jean-Paul Callot, David Grégoire

Diffusion driven barite front nucleation and crystallisation in sedimentary rocks

Bruno Leclere[a,*], Hannelore Derluyn[a,b], Eric C. Gaucher[c], Sylvain Calassou[c], Joseph Diaz[a], Jean-Paul Callot[a], David Grégoire[a,d,*]

[a] *Universite de Pau et des Pays de l'Adour, E2S UPPA, CNRS, LFCR, Anglet, France*
[b] *Universite de Pau et des Pays de l'Adour, E2S UPPA, CNRS, DMEX, Pau, France*
[c] *TOTAL CSTJF, Pau, France*
[d] *Institut Universitaire de France, Paris, France*

Abstract

–

Accepted manuscript in *Geochimica et Cosmochimica Acta.*

DOI: 10.1016/j.gca.2022.09.039.

The final publication is available at:

https://doi.org/10.1016/j.gca.2022.09.039.

–

The need to investigate mineral precipitation in heterogeneous sedimentary rock with complex pore network and mineral composition arises with problems like pore clogging by barite precipitation during sulfate-rich water injection in geological reservoirs, the durability of long term storage of nuclear waste or the damage induced by crystallisation. At the LFCR[1], we aim to reproduce geological objects in laboratory conditions. In this frame, we built

*Corresponding authors
Email addresses: bruno.leclere@univ-pau.fr (Bruno Leclere), david.gregoire@univ-pau.fr (David Grégoire)

[1] Laboratoire des Fluides Complexes et leurs Réservoirs, Anglet, France

a contra diffusive set up to precipitate a barite front in two sedimentary rock samples, a Lavoux oolitic limestone and a Vosges Sandstone with a fraction of clays. Two reservoirs filled respectively with $BaCl_2$ and Na_2SO_4 dissolved in milli-Q water are in contact with a porous sample so that the ions diffuse through it. X-ray tomography shows that a barite front is precipitated in both samples at different positions depending on the diffusion of the different ions. SEM/EDS microanalysis on polish sections highlight both the barite front location and its connectivity. In the Lavoux limestone, a connected barite front is present. Fine barite aggregates preferentially precipitate in the smallest pores of the Lavoux sample, whilst the crystals precipitating in large macropores (>20 μm) show a preferential orientation. We propose that the Gibbs free energy barrier for barite heterogeneous nucleation in the limestone is lower in contact with micrite in small pores than in contact with euhedral calcite in large pores. Finally, the Gibbs energy barrier for barite homogeneous nucleation in large pores is the highest. In the Vosges sandstone, the barite front is scattered with well-crystallized barite precipitating in large pores, and a more striking thin layer of barite is precipitated in the interfoliar space of chlorite-smectite complex. Consequently, we propose that smectite can concentrate barium by adsorption. Then because sulfate and sodium concentrations increase, ultimately barium is desorbed and barite precipitate.

Keywords: barite, diffusion, crystallisation, Lavoux limestone, Vosges sandstone, crystallisation pressure

---

1. Introduction

The understanding of the processes of reservoir clogging are of main interest for hydrocarbon reservoir management, CO_2 natural gas storage, or toxic and nuclear waste isolation. Furthermore, the precipitation of new minerals in the porosity may damage rock through the so-called *crystallisation pressure* (e.g. Scherer (2004); Steiger (2005)). This phenomenon may provoke a counter-effect onto the porosity clogging by propagating fractures (e.g. Noiriel et al. (2010); Van Noort et al. (2017)). In this case the porosity network changes from matrix porosity to fractured porosity. Another example is CO_2 storage in geological formation that causes salt precipitation, a threat for the dry CO_2 injection rate because it might clog the porosity in the vicinity of the well. However, a study reports injectivity improvement afterward (e.g. Miri and Hellevang (2016)), that might be caused by stress exerting in the porous network from salt crystallisation and eventually fracturing the clogged rock. Long-term issues may also arise with the integrity of the reservoir cap rock for long term storage of CO_2 or the geological formation for nuclear waste repositories if a stress from crystallisation could occur during the precipitation of remobilised mineral from the CO2 reservoir or nuclear waste. Finally, the precipitation of the antitiaxial veins driven by crystallisation pressure is proposed in a geological context (e.g. Elburg et al. (2002)) and some are of barite composition (e.g. Cobbold et al. (2013)). Consequently, it is essential to decipher the problem of mineral precipitation in the pores not only in term of porosity clogging but also in term of creation of new permeability drains and veins.

Thus, the aim of our study is to describe the geochemistry and geometry of mineral crystallisation in heterogeneous and porous geological rocks under the conditions where mineral crystallisation could promote crystallisation stress. For this purpose, we choose to precipitate barite ($BaSO_4$). Barite is commonly encountered in geological reservoir, where it is a clogging problem for the oil&gas production (e.g. Collins (2005)) and for the retention of radionuclides coming from the decay of nuclear waste (e.g. Klinkenberg et al. (2021)). Barite precipitation is widely studied to improve the understanding of crystal nucleation (e.g. Henisch and García-Ruiz (1986); Prieto et al. (1990); Putnis et al. (1995); Prieto (2014); Ruiz-Agudo et al. (2020)), to explore the growth rate and ontogeny of crystals of the barite group in porous media (e.g. Prieto et al. (1992); Godinho and Stack (2015); Godinho et al. (2016)), to provide solutions for inhibiting barite clogging in porous reservoirs during seawater injection. Barite has a low solubility and slow precipitation kinetics (e.g. Rajyaguru et al. (2019)) and the solution can reach high supersaturation with respect to barite (e.g. Prieto et al. (1990); Putnis et al. (1995)): the calculation of the crystallisation pressure exerted by a mineral precipitating is a function of the logarithm of the saturation of the solution, then it is interesting to precipitate barite to study pore clogging and also crystallisation stress.

With the issue of the sustainability of long-term storage of nuclear waste in deep geological repositories, concerns arise over the interaction between the nuclear waste, the cementitious materials and the surrounding clay host rock formation water (e.g. Gaucher and Blanc (2006)). In this context, barium-

rich pore water may incorporate fission product decay in the clay by barite crystallisation (e.g. Heberling et al. (2018)) and by barium sorption into clay minerals (e.g. Klinkenberg et al. (2021)). Therefore several studies focus on barite precipitation through the replacement of celestite ($SrSO_4$) dissolution (e.g. Poonoosamy et al. (2015, 2016, 2020)) and conclude on two distinct nucleation mechanisms for barite precipitation: homogeneous nucleation in the pore space and heterogeneous nucleation on the surface of a solid substrate. Epitaxial growth of barite on celestite (e.g. Poonoosamy et al. (2016)) or gypsum ($CaSO_4 \cdot H_2O$) (e.g. Forjanes et al. (2020)) is described as a rim of barite enveloping the host crystal.

A diffusion-driven reaction experiment investigating the precipitation of barite in low permeability chalk and the evolution of the transport properties concluded that the precipitation of barite is controlled by heterogeneous and homogeneous nucleation (e.g. Rajyaguru et al. (2019)). These results are relevant to describe the precipitation of barite in a neutral medium. Diffusion-driven reaction experiments precipitated celestite, a mineral of the barite group, in compacted illite. They focused on the transport of chemical species: restriction of anion diffusion in the smallest pore after celestite precipitation (e.g. Chagneau et al. (2015b); Fukatsu et al. (2017)). According to Loon et al. (2016), homogeneous nucleation happens in compacted illite as nanocrystalline celestite crystals are precipitated in the pore space. Barite precipitation in compacted kaolinite led to similar observations on anion transport and reduced barium diffusion due to barium sorption on kaolinite pores and lower self-diffusion compared to sulfate (e.g. Rajyaguru

et al. (2021)).

To address the problems of reservoir rock clogging and eventually the crystallisation-induced damage by barite, we design a counter diffusion experiment to precipitate a barite front. Analysis may be performed at a microscopic scale in order to decipher homogeneous and heterogeneous nucleation and also at a macroscopic scale in order to describe pore-clogging and possibly crystallisation pressure effect. Therefore, non-destructive X-ray microtomography scans of the reacted sample are taken to visualise the texture of the barite front precipitated in the sample porosity. In addition, observation of the front by scanning electron microscopy focuses on the crystallisation processes. The description of this type of experiment can be the support of future coupled transport chemistry numerical modelling.

2. Materials and methods

2.1. Materials

2.1.1. Lavoux limestone

The Lavoux limestone is an extensively studied limestone in the CO_2 storage field (e.g. Kalo et al. (2017); Rimmelé et al. (2010); Radilla et al. (2010)). It is a Callovian age pelletoidal, oolitic and bioclastic grainstone originating from the southwest of the Paris basin. Our samples are extracted in the Carrière de la Vienne. It is composed of oolites (micritic peloids) (100 to 1000 μm size) and echinoderm fragments cemented by syntaxial sparite cement (equant calcite) with traces of clay and dolomite. Mercury intrusion porosimetry (MIP) has been performed through an Autopore IV apparatus

(Micromeritics) and figure 1.a shows a bimodal pore size distribution with a first pore throat family centered on d_{m1} = 285 nm and a second pore throat family centered on d_{m2} = 18.6 μm. The total pore volume reaches 19.2% as indicated in table 1. The permeability of the Lavoux limestone is between 200-300 mD (e.g. Radilla et al. (2010)). According to 3D X-ray microtomography scans and observation of polish sections of the original material, the core sample is homogeneous in terms of porosity and tortuosity.

2.1.2. Vosges sandstone

The Vosges sandstone is a Triassic detrital sandstone (Rauscher Quarry, Adamsviller, France). The red color comes from ferric oxides that are alteration products of iron-rich minerals like magnetite or mica. A quantitative evaluation of the material by Scanning Electron Microscopy (QEMSCAN) provides the modal mineral distribution of the stone (% surface) (see Table 1). Minerals of the matrix are quartz, K-feldspar, and clay fractions represented by illite, kaolinite, smectite, and chlorite which are, according to the diagenetic sequence, authigenic (e.g. Blaise et al. (2016)). Blaise et al. (2016) report partly dissolved feldspar reprecipitated in illite alongside with Illite-smectite (I-S) and Chlorite-Smectite association (C-S). Pyrite is also precipitated with authigenic clay. The QEMSCAN does not distinguish illite from smectite. Meanwhile, by considering the illite, kaolinite, and chlorite fraction in our sample of Vosges sandstone, a Cationic Exchange Capacity (CEC) is calculated and ranges between 0.7-2.9 meq/ 100g for the total rock, by taking the theoretical CEC of illite and chlorite between 10-40 meq/10g and kaolinite between 5-15 meq/ 100g (e.g. Morel (1996)). The CEC of the clayish fraction is 9-35 meq/ 100g. The calculated CEC for Vosges sandstone

is coherent with the values given by Baudracco and Aoubouazza (1995), 24 meq/ 100g for the clayish fraction, and 0.98 meq/ 100g for the total rock. Consequently, because most clay mineral structures exhibit a negative charge that is balanced by an electrical double layer at the mineral water interface, the anion diffusion flux and cations migration should be restricted in the Vosges sample (e.g. Chagneau et al. (2015b)). Mercury intrusion porosimetry (MIP) has been performed through an Autopore IV apparatus (Micromeritics) and figure 1.b shows a monomodal pore size distribution with a pore throat family centered on $d_{m3} = 16.7$ μm. This family of pores corresponds to the macropore between the Quartz and K-feldspar grains. The interlayer porosity between the clay sheets is not detected by the technique. The total pore volume reaches 20.5% as indicated in table 1. According to 3D X-ray microtomography scans and observation of polish sections of the original material, the core sample looks homogeneous in terms of porosity and tortuosity. The permeability is 10.2 mD according to Baudracco and Aoubouazza (1995).

2.2. Experimental protocol

The contra diffusive experiment is set up with two reservoirs containing the same volume of solution at similar density connected with a valve to the diffusion cell, as depicted in figure 2. A density difference between two solutions at different concentrations filling opposite reservoir results in a different hydrostatic pressure in both reservoirs. This pressure difference is the driving force for the non-negligible convective transport mechanism in a permeable sample. It is characterized by a bent concentration profile as shown in the literature (e.g. Poupeleer (2007); Poupeleer et al. (2006)). To

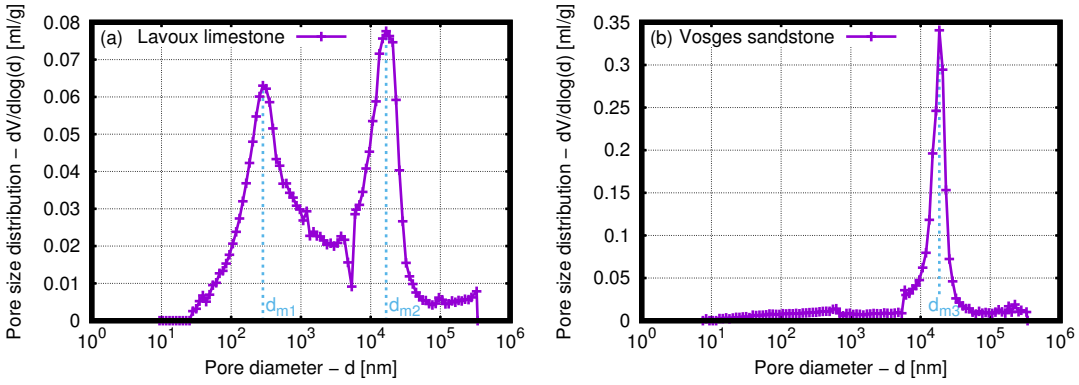

Figure 1: Pore size distributions characterized by mercury intrusion porosimetry for (a) Lavoux limestone and (b) Vosges sandstone (d_{m1} = 285 nm, d_{m2} = 18.6 μm and d_{m3} = 16.7 μm).

Table 1: Initial rock characteristics

Porous medium	Lavoux Limestone	Vosges Sandstone
Porosity*	19.2%	20.5%
Grain size	190 μm	70 μm
Modal analysis**	99.9% calcite	58% quartz, 28% K feldspar, 6.7% Illite/smectite, 1.9 % kaolinite, 1.31 % chlorite, + minor trace of muscovite, oxide (titane, ferric) carbonate, sulfur (pyrite)

*Autopore IV analysis performed by LFCR lab (Anglet, France).

**QEMSCAN analysis performed by Total CSTJF lab (Pau, France).

minimize transport by convection based on density difference between electrolytes (e.g. Poupeleer (2007); Poupeleer et al. (2006)), the concentration in reservoir B is fixed at 0.5 molal of Na_2SO_4 while the concentration in reservoir A is 0.34 molal of $BaCl_2$.

The density of a 0.5 molal Na_2SO_4 solution is 1.0573 at 25^oC and 1.0590 at 20^oC (e.g. Millero et al. (1977); Krumgalz et al. (2000)). The solution is prepared by adding 7.1 gram of Na_2SO_4 to a volume of 100 ml of pure water. The density of a 0.34 molal $BaCl_2$ solution is interpolated according to the value measured by Puchalska and Atkinson (1991) (the density at 25^oC is 1.0578). The solution is prepared by adding 8.32 gram of $BaCl_2$ to a volume of 98.7 ml of pure water at 25^oC and 1 atm.

The diffusion cell consists of a porous rock sample, beforehand washed with deionized water, clamped between two stainless steel inlets, and confined with a heat shrinkable covering with adhesive. The distance between the sample and the reservoirs is set at 8 cm. The dimensions of each rock sample are given in table 2. Two experiments are reported with two different porous media: a Lavoux limestone and a Vosges sandstone. The contra diffusive test with Lavoux oolite limestone is denoted BF_L for Barite Front Lavoux. The test with Vosges sandstone is denoted BF_V for Barite Front Vosges. With this experiment, we aim to precipitate a barite front ($BaSO_4$) in the porous rocks by contradiffusion of the Ba^{+2} rich $BaCl_2$ dissolved solution and the SO_4^{2-} rich Na_2SO_4 dissolved solution.

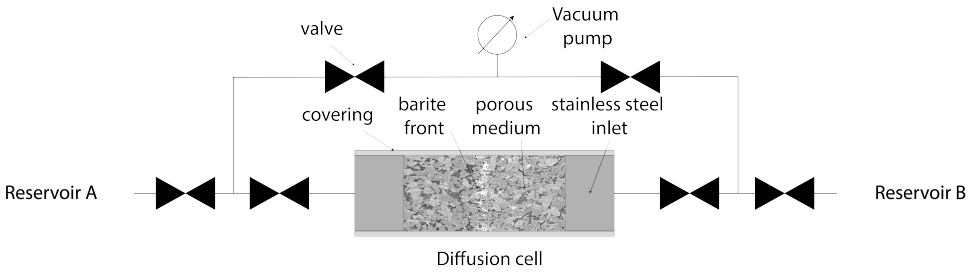

Figure 2: Experimental set-up. The core sample assembled with stainless steel inlet at both sides is tightened in a heat shrinkable covering with adhesive. The cell is located at an equal distance between the reservoir containing the solutions and tightly connected with PFA tubing of $\frac{1}{4}$ inch and valves (Swagelok). A vacuum pump, PK D57 712 (Pfeiffer vacuum) is connected to remove air from the circuit before saturating the circuit with the solutions.

The diffusion cell is prepared by fully saturating the cell and the sample inside with deionized water following the European standard EN 1936: *(i)* the diffusion cell is placed vertically in a vacuum bell jar connected to a vacuum pump during at least 2 hours at 2 kPa to fully empty the sample. *(ii)* Pure water (Milli-Q from Millipore, 18 MΩ cm at 20^{o}C) is slowly added until the top of the cell is covered. 2 kPa needs to be maintained during 15 min after adding the water. *(iii)* The diffusion cell is kept at atmospheric pressure during at least 24 hours. The diffusion cell is then connected to the reservoirs using tubing of an equal length separated by a valve and a vacuum pump. Before opening the reservoir valves, the tubing in between the reservoir valve and the cell valve is emptied for a couple of minutes and the vacuum pump valve closed. Then the valves are open and the electrolytes saturate the tubing between the reservoir and the diffusion cell valves. The absence of air bubbles is controlled. Finally, the valves on both sides of the

diffusion cell are opened simultaneously.

The duration of each experiment is set according to simulations computed on Phreeqc (e.g. Parkhurst et al. (2013)) ensuring that the simulated saturation in the sample reached the experimentally measured supersaturation threshold obtained with similar starting concentrations in silica gel (e.g. Putnis et al. (1995)). The simulation is provided as supplementary data.

Table 2: Sample dimensions and experimental conditions.

Exp. reference	Rock type	Diameter	Length	Duration
BF_L	Lavoux limestone	25 mm	38 mm	66 days
BF_V	Vosges Sandstone	6.9 mm	25 mm	75 days

At the end of the test, the valves are closed and the sample is disconnected from the reservoirs. The sample is then dried and characterized using different techniques described in the next section. Two experiments are reported in this paper with two different porous media in Table 2.

2.3. Characterization methods

2.3.1. X-Ray micro tomography

A Bruker Skyscan 1172 (UMS 3360 DMEX, UPPA) is employed to acquire X-ray microtomography scans of the rock samples and investigate the precipitated barite front and the microstructure of the porous medium in 3D. One post-mortem scan of the barite front precipitated in Lavoux is taken at a resolution of 9.95 μm and one post mortem scan of the barite front in the Vosges sandstone is taken at a resolution of 3.27 μm. Scans are acquired at an energy of 100 kV, 2000 projections are taken over 360°, from which

the 3D volume is reconstructed using a classical back-projection algorithm. The grey values in the reconstructed images reflect how strongly X-rays are attenuated by the sample. The attenuation by a mineral or fluid is a function of its atomic number and its density: the heavier, the more it will attenuate. Low grey values (dark voxels) correspond to low attenuation and thus light elements, whereas high grey values (bright voxels) reflect higher attenuation and thus heavier elements. Therefore, in our images, pores appear dark while the skeleton of the porous medium appears greyish. In the skeleton, barium has the highest atomic number, and therefore barite minerals will appear as the brightest phase in the image.

2.3.2. SEM-EDS and QEMSCAN

A Scanning Electron Microscope, SEM-FEG Quanta 650 FEI (TOTAL CSTJF lab, Pau, France), coupled with microanalysis Energy Dispersive X-ray Spectroscopy (EDS) (Bruker X-Flash) is used to investigate the chemical and microstructural changes in the porous media. Measurements are undertaken using a backscattered electron (BSE) detector in vacuum mode at an accelerating voltage of 15 kV and a working distance of 13 mm. Since heavier atoms return more backscattered electrons they appear brighter. This explains the phase contrast between barite and the other minerals constituting the porous medium.

2.3.3. Thin section and polished section

Thin Section Lab (Toul, France) prepares the thin sections of the original rock samples with the following protocol: impregnation with epoxy resin, sawing, and polishing with pure water. For the preparation of polished sam-

ples of the rocks after the contra-diffusion experiment, which we further refer to as reacted samples, the dried-out samples are first impregnated with epoxy before being saw with a mineral oil lubrification. A second impregnation with epoxy precedes the polishing. *Thin section Lab* prepared the polished section of reacted Lavoux limestone and the thin section of reacted Vosges sandstone was prepared at the LFCR laboratory (UMR 5150, UPPA, Pau, France).

3. Results

3.1. Lavoux limestone experimental results

A precipitated barite front is located 6 to 10 mm from the barium source side (Lavoux sample length is 38 mm), as shown in the radiography (figure 3). It is the thin, 10-20 μm, dark slightly bent line separating the sample. Figure 4 zooms in on the front, showing a cross-section of the 3D reconstructed volume. The dotted line delimitates a zone where barite crystallites are precipitated inside the pores. We remark that the pores located on the barium source side are brighter than on the sulfate side because they are saturated with the barium-rich solution, which attenuates the X-rays more strongly than the sulfate solution.

A 3D visualization of the front (figure 4b), confirms the previous observation. The front shape is a bumpy surface and the barite front is fraying in the direction of the barium source side.

In SEM-EDS analysis, barite precipitates are visible as a whitish connected front (Figure 5.a) and as isolated crystals precipitated inside large pores on the barium source side (figure 5.b). Large pores (>20 μm) across the barite front path contain larger crystals (figure 5.c). Xenomorphic barite pre-

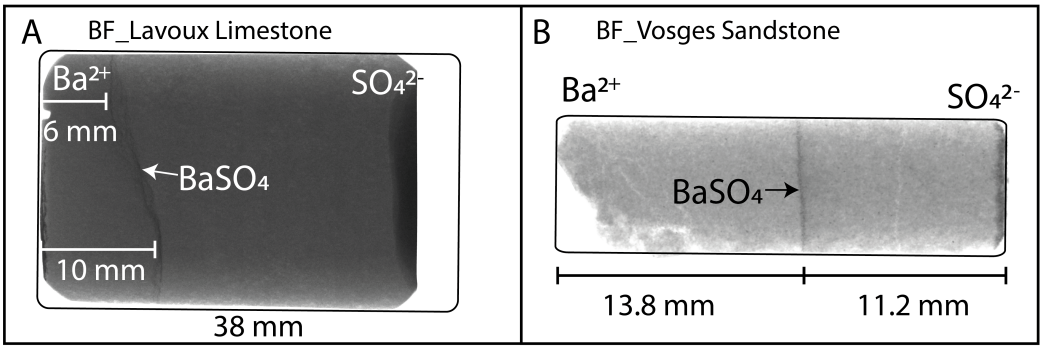

Figure 3: Bruker Skyscan 1172 X-ray radiography A) BF_L at a 9.95 μm resolution, B) BF_V at a 3.27 μm resolution.

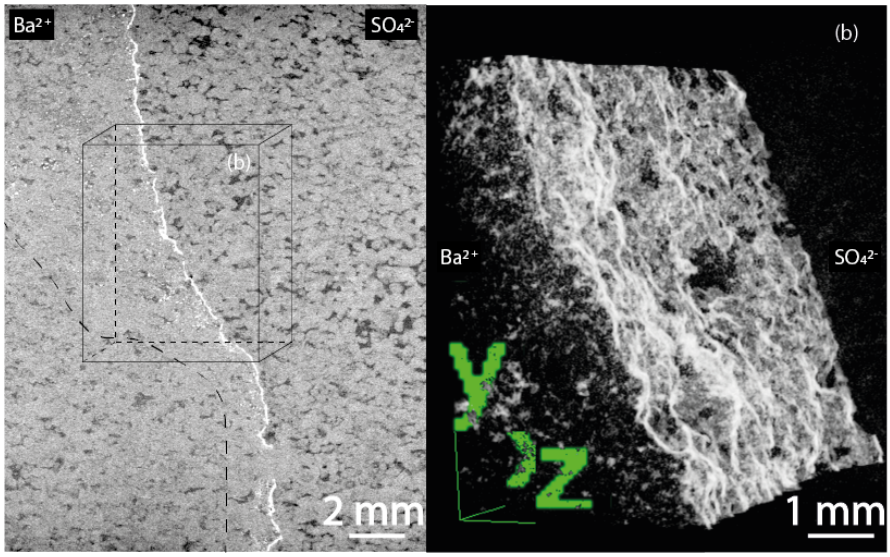

Figure 4: X-ray tomography analysis of sample BF_L. (a) 2D frontal cross-section centered on the barite front (white) precipitated in the porosity (dark grey). Isolated barite crystal are visible on the left of the principal barite front. (b) 3D visualization of the barite front.

cipitated preferentially in contact with micrite constituting the oolite along the barite front (figure 5.d). A focus on an inter oolitic pore in which small crystallites are precipitated shows that the nucleation happens preferentially on micrite, rather than on the sparite cement or euhedral calcite (figure 5.b).

In the upper part of the polished section (figure 5.a), the front separates into two paths which are highlighted as barite front fingering in figure 5.e & f. The direct path crosses a large pore (≈50 μm) where a large crystal is oriented perpendicularly to the pore wall (figure 5.f). The indirect path contains crystallites precipitating in contact with micrite and does not cross through the large inter-oolites pores (figure 5.e & f).

3.2. Vosges sandstone experimental results

3.2.1. Description of thin sections of non-reacted Vosges sandstone

The analysis of BSE 300 nm and EDS 3 μm interpreted by QEMSCAN complete the information provided by Blaise et al. (2016) on clay particles. EDS 3 μm interpreted by QEMSCAN evidenced precipitated kaolinite as blocky dickite-like crystals or intercalated between the illite layering forming the K-I complex, as shown in figure 6a & b. Chlorite is associated with smectite. A whitish mineral is precipitated in the void identified as a trace of ferric oxide or ferrihydrite (figure 6a & c). A chlorite-smectite complex (C-S) is torn apart by the adsorption-induced swelling of hydrated cations, a transformation from smectite to chlorite by the addition of a brucite layer, and possibly the precipitation of a ferrihydrite (figure 6a & d). It is worth noting that there is an affinity for ferrihydrite to precipitate in contact with chlorite (e.g. Brandt et al. (2012)).

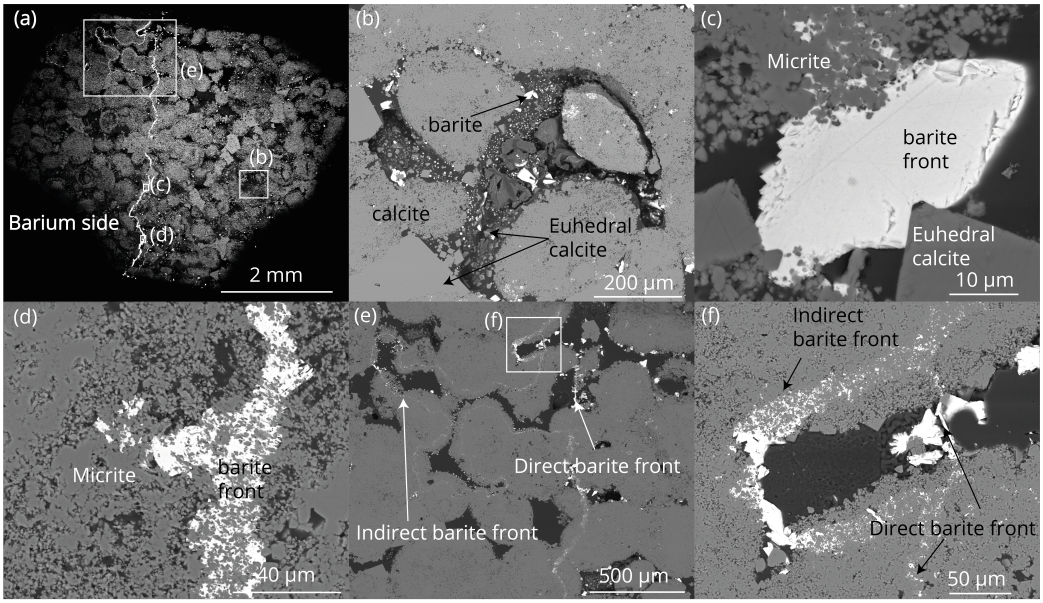

Figure 5: SEM-BSE observations on BF_L. (a) barite front highlighted; barite front separation (direct and indirect) in the top of the SEM-BSE image, barite crystals precipitated in the porosity on the Ba side. (b) large pore localized away from the front in the barium side with barite crystals seeded on micrite. (c) large barite crystal on the barite front clamped between pseudomorphic calcite and micrite of oolite grains. (d) barite front precipitated in contact with micrite constituting oolite grains. (e) barite front fingering. (f) direct and indirect barite front in the fingering area; large barite in a large pore oriented perpendicularly to the pore wall.

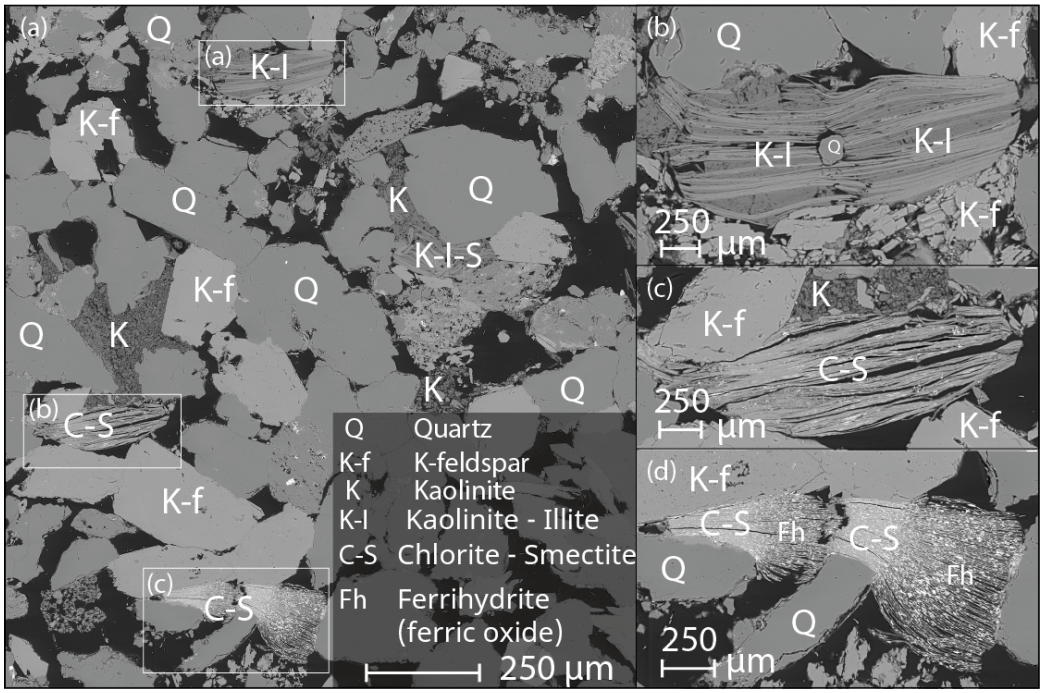

Figure 6: BSE 300 nm of thin section of Vosges sandstone with details on clay particles. (a) representative overview of Vosges sandstone composition. Quartz and K-feldspar are the major elements followed by kaolinite, authigenic illite and chlorite - smectite complex. (b) inter stratified illite and kaolinite precipitated around a quartz grain. (c) inter stratified chlorite-smectite. (d) Peeled inter stratified chlorite-smectite filled with ferric oxide or ferrihydrite (interpreted EDS 3 μm).

3.2.2. Barite front precipitation in Vosges sandstone

A half millimeter-thick barite vertical front is precipitated after 75 days contra-diffusion of the two solutions at 13.8 mm of the barium source side (Vosges sample length is 25 mm) as shown in figure 3. On a vertical cross-section from X-ray tomography datasets centered on the barite front, figure 7 shows that the front is disconnected. Isolated barite crystallite fills the pores between the quartz and K-feldspar grains (light grey level) and inside the illite/smectite complex. However, the barite crystals are not connected like the barite front precipitated in the Lavoux limestone. Dissolved ions in solution contribute to the absorption of X-rays and thus the barium chloride side appears lighter than the sodium sulfate side due to the higher attenuation by barium compared to the other ions in solution. This is revealed by the horizontal normalized mean grey value calculated with ImageJ (Figure 7).

SEM-BSE data are acquired on the polished section to enhance the understanding of the barite precipitation. An SEM-BSE overview of the polished section combined with EDS microanalysis allows distinguishing three cases of precipitation. Firstly, barite precipitate as well-crystallized crystals in the larger pores. Secondly, barite precipitate in contact with clay and especially with the chlorite-smectite complex. Thirdly, small barite crystallites are found in contact with dickite-like kaolinite, as illustrated in figure 8.

Zoom in the barite precipitated in contact with clay revealed that nanometric barite precipitated in the voids between the layers of the chlorite-smectite complex as shown in figure 9.

Barite and ferric oxide interlayered in the chlorite-smectite complex are identified with EDS microanalysis on a 1-3 μm^3 volume of material (Bruker

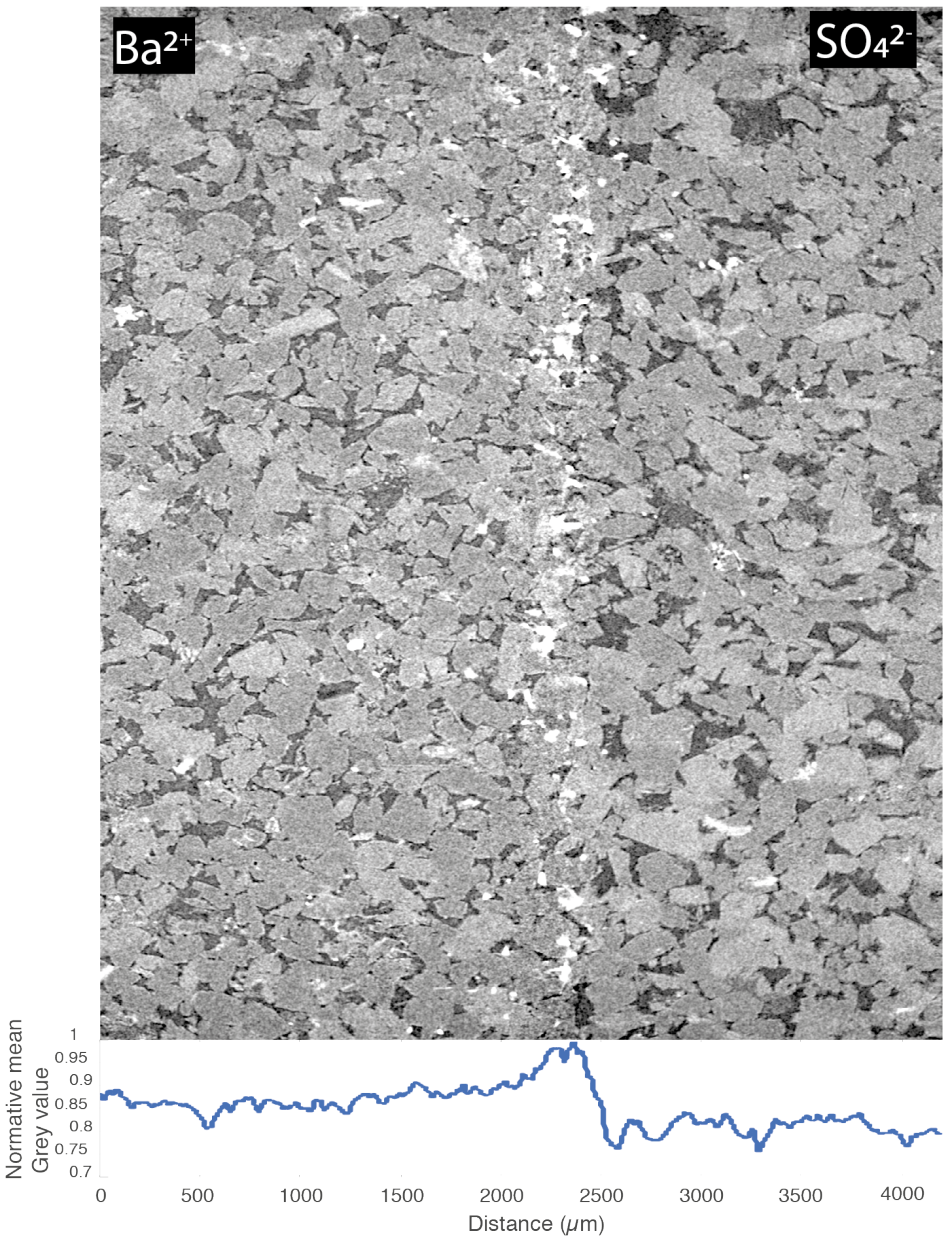

Figure 7: X-ray tomography vertical cross section of sample BF_V processed with ImageJ (top) 2D frontal cross-section centered on the barite front (white) precipitated in the porosity (dark grey) between feldspar, clay and quartz grains (light grey). (bottom) normalized mean grey values are obtained versus the horizontal axis by summation of the cross-section image pixel along the vertical axis.

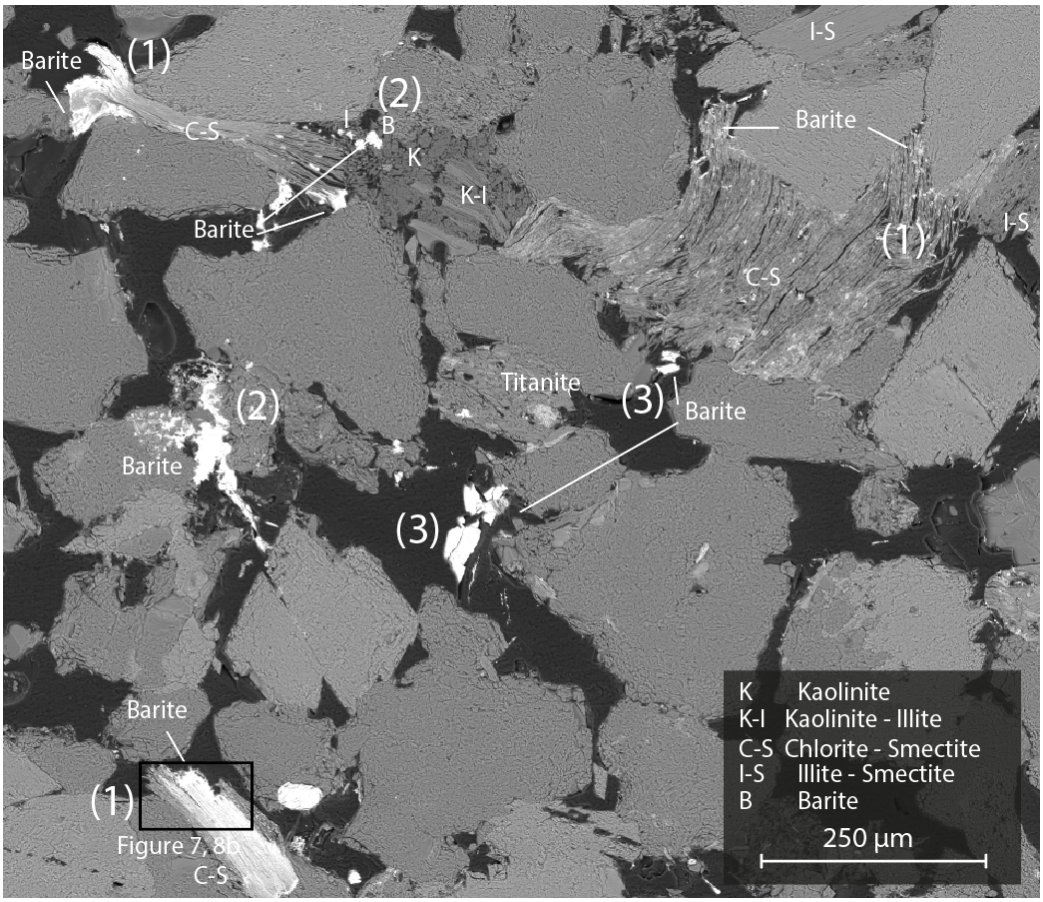

Figure 8: Barite occurrences observed and interpreted with SEM BSE acquired on the BF_V sample polished section. (1) Barite precipitate predominantly in contact with chlorite-smectite complex. (2) Small barite crystallites precipitate in contact with dickite like kaolinite. (3)Large barite crystals are observed in the larger pores with no clear contact with the clay complex.

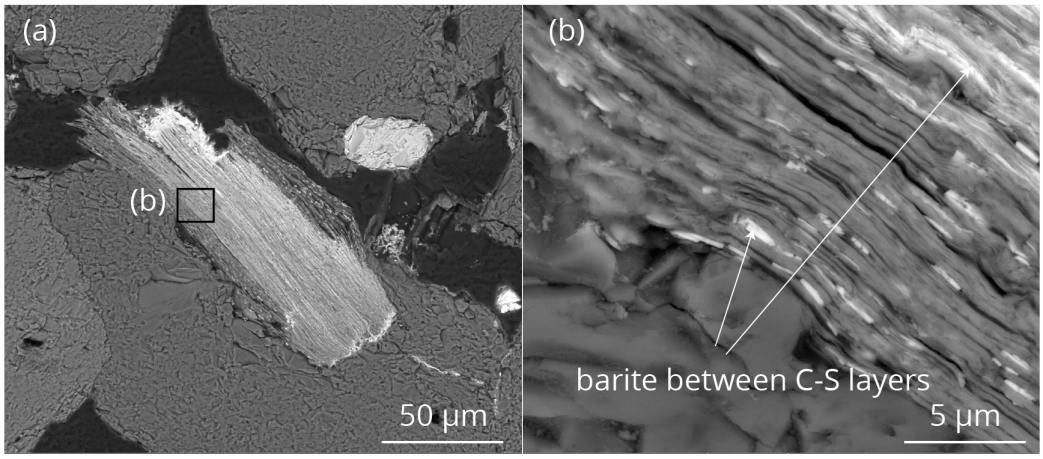

Figure 9: SEM BSE images of BF_V. (a) cross sectional overview of a C-S complex with barite precipitated in contact. (b) thin barite layer precipitated between C-S layer

X-Flash as shown in figure 10).

4. Discussion

4.1. Barite front position in Vosges sandstone and Lavoux limestone

The positions of the barite front across the length of the samples differ between the samples. The transport by diffusion of a chemical specie in a porous medium is described by the second Fick's law:

$$\frac{\delta C}{\delta t} = \frac{D_e}{\epsilon} \cdot \frac{\delta^2 C}{\delta^2 x} \ . \tag{1}$$

In Eq. 1, D_e (m^2/s) is the effective diffusion coefficient of the chemical species, ϵ the accessible porosity and C the concentration (molal). Pure diffusion conditions of the electrolytes are modeled with Phreeqc (e.g. Parkhurst et al. (2013)). It results that the barite supersaturation curves top at 18-19 mm of the barium side in the Lavoux limestone and 12 mm of the barium side

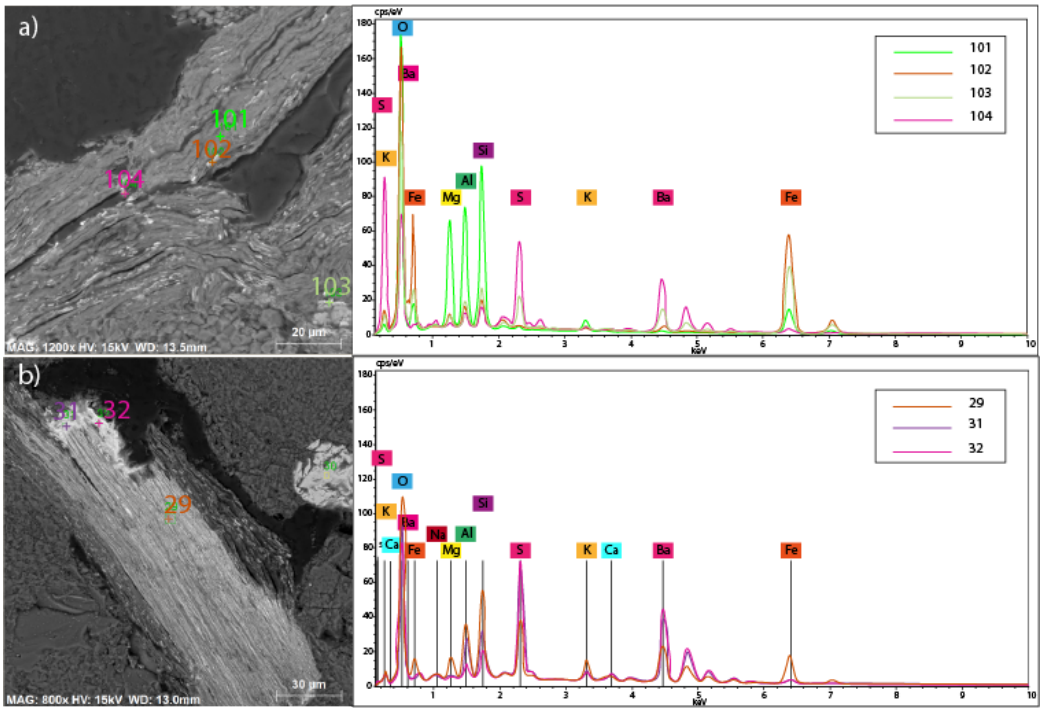

Figure 10: EDS micro analysis of BF_V on a 1-3 μm^3 volume of material (Bruker X-Flash). (a) chlorite-smectite complex (101), ferric oxide (102), mix of ferric oxide and barite interlayered in C-S complex (103), Barite (104). (b) mix of ferric oxide and barite interlayered in C-S complex (29, 31, 32).

in the Vosges sandstone. The comparison with the experimental data shows that the barite front is ∼10 mm shifted to the barium side in the Lavoux limestone and ∼2 mm shifted to the sulfate side in the Vosges. Then, there are other parameters to consider that are related to chemical interaction with the porous medium like adsorption and precipitation. An additional term is added in the second Fick's law: $\rho_s \cdot \frac{\delta \bar{C}}{\delta t}$ with ρ_s the volumetric mass density of the dry sample (kg/m^3) and $\bar{C} = K_d \cdot C$ with K_d the distribution coefficient.

4.2. Ionic diffusion in clay-rich host rock.

To describe the effect of adsorption on the ionic diffusive transport in clay-rich porous media, it is necessary to distinguish the transport of cations (charged positively) and anions (charged negatively).

For the diffusion of the cation, Rajyaguru et al. (2021) measure a reduction in the barium diffusion in a sample of kaolinite saturated with Na^+ during the counter-diffusion of two electrolytes with a concentration 100 mmol.L^{-1} NaCl and 4 mmol.L^{-1} Na_2SO_4 and $BaCl_2$. Melkior et al. (2009) measures an acceleration of Na^+ diffusion when there is a homogeneous gel structure in pure Na-smectite and in low concentration solution ($\sim 10^{-3}$ molal).

For the negative charge of the anions, their diffusion is restricted in the vicinity of the clay particles charged negatively by the electric double layer of the TOT (tetrahedral-octahedral-tetrahedral) layers. This effect is reported for $^{36}Cl^-$ by Fukatsu et al. (2017) and Chagneau et al. (2015b).

The samples used by Melkior et al. (2009) and Chagneau et al. (2015b) are respectively 80% and 70% rich in clay equilibrated with a sodium solution beforehand. Rajyaguru et al. (2021) kaolinite is saturated with Na^+.

By comparaison, the experimental Vosges sample contains up to 10% of clay and Na^+ balancing was not carried out before diffusion. Therefore, the clay adsorption site is occupied by a variety of cations. The electrolytes are concentrated two order of magnitude more than Melkior et al. (2009) and Rajyaguru et al. (2021).

The shifted position of the barite front towards the sulfate inlet observed in this study seems to contradict the observation of Rajyaguru et al. (2021). On the other hand, the cations diffusion accelerations of Melkior et al. (2009) are not applicable since the experimental rock is not equilibrated with a cation to have homogeneous gel structure in the smectite. At least the results of Fukatsu et al. (2017) and Chagneau et al. (2015b) regarding the reduced diffusion of anions could be considered if the presence of 10% of clay would be sufficient to influence their diffusion. Thus the position of the barite front in the Vosges is still debated as to the influence of the clay fraction on the ionic diffusion.

In addition, the adsorption of cations in the interfoliar space of the clay and the precipitation of barite play a role at a another level: it partly consumes the barium by adsorption on clay and on an equal level barium and sulfate by precipitation of barite. Precipitation of the barite front may also further limit the diffusion of sulfate (e.g. Chagneau et al. (2015b)).

4.3. Diffusive vs convective transport mode

All experiments are conducted with care to ensure only diffusive transport conditions. However, in BF_L the bending of the barite front, the presence of isolated barite crystals fraying on the barium source side and the position of the front shifted to the barium side might belong to advective transport

features. These features are not recognized in BF_V. Despite the care taken, there could be a slight pressure difference in BF_L when the diffusion starts and/or when the diffusion stops by operating the valve leading to a combination of diffusive and convective flow (e.g. Poupeleer (2007); Poupeleer et al. (2006)).

4.4. Model for barite nucleation in a bimodal heterogeneous pore network

The medium tested here being more heterogeneous than the silica gel used in Putnis et al. (1995), Prieto et al. (1990, 1992) or Henisch and García-Ruiz (1986), the heterogeneous nucleation conditions are linked to the different surface morphology of the calcite in contact which barite nucleates (e.g. Grosfils and Lutsko (2021)) and pore size (e.g. Prasianakis et al. (2017); Putnis and Mauthe (2001)). Because no barite rim are observed and the lattice mismatch between barite and calcite is high, ≈ 80 % (e.g. Downs and Hall-Wallace (2003)), the hypothesis of epitaxial growth of barite on calcite is not relevant like in similar experiment (e.g. Rajyaguru et al. (2019)). In large pore of diameter greater than 1 μm homogeneous nucleation is likely to occur because a supercritical barite cluster can potentially form in the pore solution and nucleate (e.g. Prasianakis et al. (2017); Rajyaguru et al. (2019)). This leads to different supersaturation thresholds in agreement with the conclusion of Rajyaguru et al. (2019): large crystals nucleate by homogeneous nucleation in macropores when a supercritical barite cluster overcomes the interfacial energy barrier of homogeneous nucleation and nucleate as a stable crystal. Classical nucleation theory assesses that this occurs when the solution exceeds the barite supersaturation threshold (e.g. Prieto (2014)). The direct observation of homogeneous nucleation could be the automorphic

barite crystals visible in figure 5. c, e & f). They are precipitated in large pores, have no contact with the calcite substrate and even show preferential orientation parallel to the direction of the barite front.

Compared to macropores, the probability of homogeneous nucleation in small micritic pores (< 1 μm) is much lower. However, the majority of barite crystal precipitate in microporosity which means that barite nucleated rather by heterogeneous nucleation in micritic pores than homogeneous nucleation.

According to Henisch and García-Ruiz (1986); Putnis et al. (1995); Prieto et al. (1990) and modeling of the experiment with Phreeqc (e.g. Parkhurst et al. (2013)), the solution supersaturation curve through the medium has a Gaussian shape. The supersaturation threshold is overcome locally and barite nucleate in the interval where the supersaturation profile crosses the supersaturation threshold.

In bimodal porosity medium, such as micritic chalk used in Rajyaguru et al. (2019) , two supersaturation thresholds are defined for barite nucleation: S_1 in small intermicrite pores (0.1-1 μm) and S_3 in macropores. In the Lavoux limestone, S_2 is defined to account for barite precipitated on contact with euhedral calcite crystals. Euhedral calcite crystals have a smoother surface than micrite which offers fewer nucleation sites and therefore requires a higher energy of activation for barite precipitation (e.g. Grosfils and Lutsko (2021)).

A conceptual model is proposed to recap the precipitation of barite in figure 11: according to the classical nucleation theory, nucleation of barite occurs when the solution saturation regarding barite reaches the dedicated supersaturation threshold. During nucleating and growing, the barite crystal will consume the ions in the solution and reduce the solution saturation.

Some questions remain whether the barite front started from one or multiple seeding crystals, the duration of the front precipitation, whether the barite front after being connected continued to increase in thickness and at how fast or whether the front acted like a permeability barrier as we propose in our conceptual model and observed on another note in Chagneau et al. (2015b,a); Fukatsu et al. (2017).

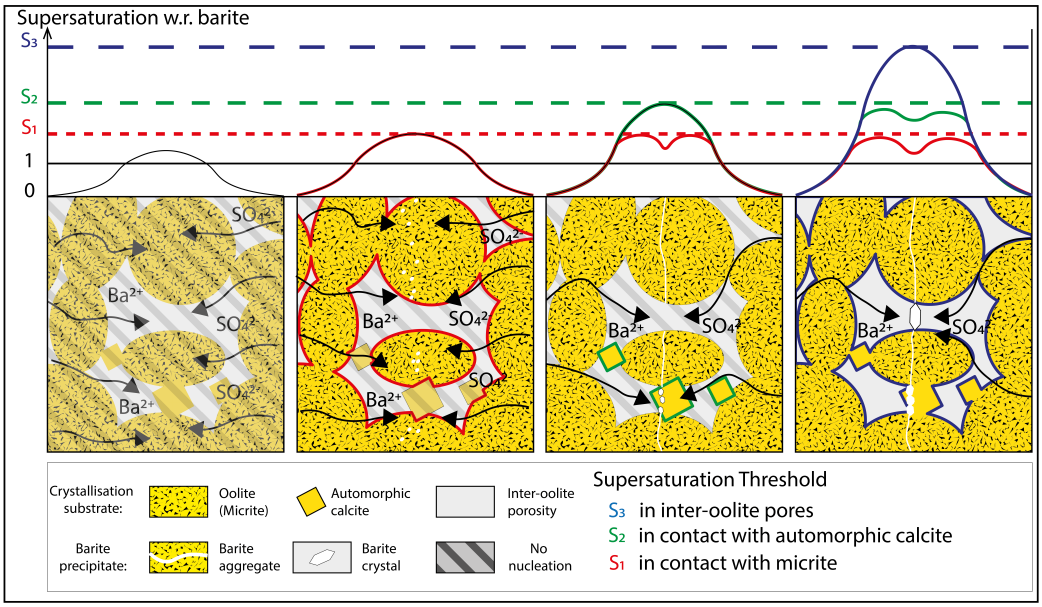

Figure 11: Conceptual model of barite precipitation in an oolite limestone. 0) supersaturation increase in the porous rock. 1) $BaSO_4$(cr) nucleate in contact with micrite when S reaches S_1, clog the small pores inside oolites along the precipitating front and reduce the ionic diffusion in the oolites. 2) $BaSO_4$(cr) nucleate in contact with sparite when S reaches S_2 3) $BaSO_4$(cr) nucleate in the macropore (Bulk) when S attains S_3 and reduce the ionic diffusion through the macropores

4.5. Model for barite nucleation in contact with smectite

In macropores of the Vosges sandstone, barite precipitates as well-formed crystals. The crystal are formed by homogeneous nucleation when a barite cluster convert into a stable nucleus (e.g. Rajyaguru et al. (2019)). The lattice mismatch between barite and K-feldspar is $\approx 4\%$ (e.g. Downs and Hall-Wallace (2003)), then theoretically, epitaxial growth of barite onto K-feldspar is likely to happen even if it was not observed.

The precipitation of barite in the interfoliar void in the clay complex is a novelty and could be driven by cation exchange in clay sheets (e.g. Atun and Bascetin (2003); Gaucher et al. (2009); Klinkenberg et al. (2021)). Gaucher et al. (2009) gives the illite/smectite selectivity coefficient for exchange reactions with a cation exchanger. The cations adsorbability ranking according to the selectivity coefficients: is : $K^+ < Na^+ < Fe^{2+} < Ca^{2+}$ & $Mg^{2+} < Sr^{2+}$. Note that this ranking might be extrapolated to barium which would have a higher affinity to adsorb onto illite/smectite minerals because it is a heavier alkaline earth cation.

In the reacted Vosges sandstone, illite is not expanded but in chlorite-smectite complex, the basal space is expanded letting barium adsorption. Barium concentration increases and become more favorable than other cations to adsorb onto smectite that is why barium replace cations adsorbed between TOT smectite layers according to the reaction, illustrated in figure 12, left.

The barium concentrate on the surface of smectite TOT and in the interfoliar void. It causes the precipitation of barite at the surface of the

delaminated TOT layer where sulfate and sodium can diffuse because the expansion of the basal space minimizes for sulfate, the anion exclusion effect describes in Chagneau et al. (2015b,a); Fukatsu et al. (2017). As the diffusion continues, the concentration of sodium increases, while barium is consumed by adsorption onto smectite and by barite precipitation in macropores. The ion exchange equilibrium turns in favor of sodium that is adsorbed in replacement of barium on the TOT sheets and because the solubility of barite is extremely low, barium and sulfate combines immediately to form barite according to reaction, illustrated in figure 12, right.

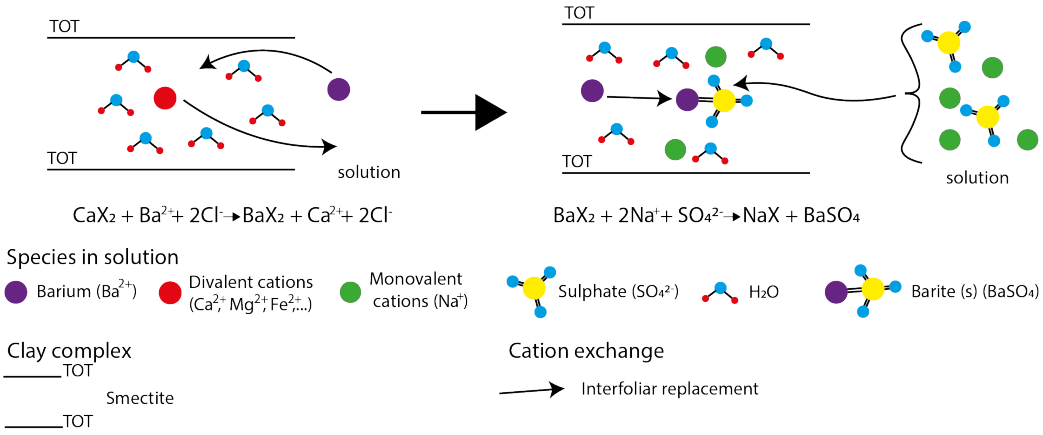

Figure 12: Conceptual model for barite precipitation in contact with smectite: 1) Concentration of barium between the TOT layer: a divalent cation is desorbed and replaced by barium between the TOT layer of smectite while the concentration of barium in solution increase. 2) Precipitation of barite: the concentration of sulfate and sodium increases. Sodium is adsorbed on the TOT sheet and sulfate captures the barium desorbed to precipitate barite in the TOT interlayer.

4.6. Implication for barite precipitation in geological environment

The experimental results on barite crystallisation in natural porous rock show:

- barite nucleation involves homogeneous and heterogeneous nucleation processes in porous rocks,
- clogging of the pore network by the barite front precipitation,
- concentration of barite precipitate in contact with C-S mineral.

In addition, the conclusion of Putnis and Mauthe (2001) and Prasianakis et al. (2017) state that the nucleation activation energy is inversely proportional to the pore size. It involves that clay minerals with nanoporosity and significant adsorption capacity are good candidates for hosting damage by crystallisation pressure. Indeed the poral solution can reach high supersaturation with respect to precipitating mineral and the onset of crystallisation in this medium would generate high crystallisation pressure. Regarding the samples, no cracks are generated in both porous media, however, the chlorite—smectite with barite precipitate in the interfoliar space depicts a swelling effect in figure 9 b and c. On the thin section of original Vosges sandstone, the precipitation of ferrihydrite in the interfoliar space led to the breakage of a chlorite—smectite sheets in figure 6,d. To resume, crystallisation can induce swelling and breakage of the clay sheets. These effects on a longer duration may generate cracks in the porous medium and a secondary fractured porosity network. In the field, fibrous veins in clay-rich formation are often related to crystallisation pressure like in Elburg et al. (2002): antitaxial fibrous calcite veins in carbonaceous shale formation of Oppaminda

creek form by crystallisation pressure and the nutrients are provided by diffusion to the precipitation site. The similarities with barite precipitated in these experiments suggest that these geological veins are the natural continuation of similar processes during a longer period.

5. Conclusion

We report first experimental results on the precipitation of barite inside two porous rocks by contra-diffusion of $BaCl_2$ and Na_2SO_4 solutions. Post mortem SEM-BSE imagery reveals, in the Lavoux limestone, that a thin continuous barite aggregate film (10-20 μm) precipitates preferentially in contact with micrite than euhedral calcite and macropores where barite crystals are euhedral. In the Vosges sandstone, euhedral crystals precipitate in macropores and barite is concentrated as an aggregate between TOT sheets of chlorite-smectite complex. We propose that the crystallisation of barite in sedimentary rock has multiple Gibbs free energy barriers governed by the different morphology of the host matrix mineral-like (for example micrite or euhedral calcite in the Lavoux limestone) and by the matrix pore size. In smectite-rich rocks, like the Vosges sandstone, barium is concentrated by ion exchange on smectite TOT sheets and then combined with sulfate. As a consequence barite precipitates between TOT sheets with an increase of the chlorite-smectite volume. Our experiment illustrates both the clogging of the matrix porosity with a barite precipitation front and the minor effect of *crystallisation pressure* when the barite precipitates inside the clay sheets. Some questions remain, namely the process(es) behind the position of the barite front in the Vosges sandstone and at the microscale if the barite front

precipitation would propagate from a single barite seed or from several seeds and if an additional process such as the generation of an amorphous precursor of $BaSO_4$ could occur during homogeneous nucleation in porous medium.

Acknowledgements

This research was partly funded by TOTAL SA and the *Investissement d'Avenir* French programme (ANR-16-IDEX-0002) under the framework of the E2S UPPA hub Newpores. We would like to thanks Total petrographic laboratory (Melanie Vauthrin & Isabelle C. Jolivet) for help in SEM/EDS analysis and B. Fasentieux (UPPA) for the conception of the polish sections.

Appendix A. Supplementary Material

Supplementary Material includes a Phreeqc modelling of a contra-diffusive experiment with the full script (part A1) and results (part A2) in term of barite supersaturation profile for both the Lavoux limestone sample (Figure S1) and the Vosges sandstone sample (Figure S2).

References

Atun, G., Bascetin, E., 2003. Adsorption of barium on kaolinite, illite and montmorillonite at various ionic strengths. Radiochimica Acta 91, 223–228.

Baudracco, J., Aoubouazza, M., 1995. Permeability variations in berea and vosges sandstone submitted to cyclic temperature percolation of saline fluids. Geothermics 24, 661–677.

Blaise, T., Clauer, N., Cathelineau, M., Boiron, M.C., Techer, I., Boulvais, P., 2016. Reconstructing fluid-flow events in lower-triassic sandstones of the eastern paris basin by elemental tracing and isotopic dating of nanometric illite crystals. Geochimica et Cosmochimica Acta 176, 157–184.

Brandt, F., Schäfer, T., Claret, F., Bosbach, D., 2012. Heterogeneous formation of ferric oxide nanoparticles on chlorite surfaces studied by x-ray absorption spectromicroscopy (stxm). Chemical Geology 329, 42–52.

Chagneau, A., Claret, F., Enzmann, F., Kersten, M., Heck, S., Madé, B., Schäfer, T., 2015a. Mineral precipitation-induced porosity reduction and its effect on transport parameters in diffusion-controlled porous media. Geochemical transactions 16, 1–16.

Chagneau, A., Tournassat, C., Steefel, C.I., Bourg, I.C., Gaboreau, S., Esteve, I., Kupcik, T., Claret, F., SchaÌĹfer, T., 2015b. Complete restriction of 36cl–diffusion by celestite precipitation in densely compacted illite. Environmental Science & Technology Letters 2, 139–143.

Cobbold, P.R., Zanella, A., Rodrigues, N., Løseth, H., 2013. Bedding-parallel fibrous veins (beef and cone-in-cone): Worldwide occurrence and possible significance in terms of fluid overpressure, hydrocarbon generation and mineralization. Marine and Petroleum Geology 43, 1–20. URL: http://dx.doi.org/10.1016/j.marpetgeo.2013.01.010, doi:10.1016/j.marpetgeo.2013.01.010.

Collins, I.R., 2005. Predicting the location of barium sulfate scale formation

in production systems, in: SPE International Symposium on Oilfield Scale, OnePetro. pp. SPE–94366–MS.

Downs, R., Hall-Wallace, M., 2003. The american mineralogist crystal structure database. American Mineralogist 88, 247–250.

Elburg, M.A., Bons, P.D., Foden, J., Passchier, C.W., 2002. The origin of fibrous veins: constraints from geochemistry. Geological Society, London, Special Publications 200, 103–118.

Forjanes, P., Astilleros, J.M., Fernández-Díaz, L., 2020. The formation of barite and celestite through the replacement of gypsum. Minerals 10, 189.

Fukatsu, Y., Van Loon, L.R., Shafizadeh, A., Grolimund, D., Ikeda, Y., Tsukahara, T., 2017. Effect of celestite precipitation in compacted illite on the diffusion of hto, 36cl-, and 22na+. Energy Procedia 131, 133–139.

Gaucher, E.C., Blanc, P., 2006. Cement/clay interactions–a review: experiments, natural analogues, and modeling. Waste Management 26, 776–788.

Gaucher, E.C., Tournassat, C., Pearson, F., Blanc, P., Crouzet, C., Lerouge, C., Altmann, S., 2009. A robust model for pore-water chemistry of clayrock. Geochimica et Cosmochimica Acta 73, 6470–6487.

Godinho, J.R., Gerke, K.M., Stack, A.G., Lee, P.D., 2016. The dynamic nature of crystal growth in pores. Scientific Reports 6, 1–7.

Godinho, J.R., Stack, A.G., 2015. Growth kinetics and morphology of barite crystals derived from face-specific growth rates. Crystal Growth & Design 15, 2064–2071.

Grosfils, P., Lutsko, J.F., 2021. Impact of surface roughness on crystal nucleation. Crystals 11, 4.

Heberling, F., Metz, V., Böttle, M., Curti, E., Geckeis, H., 2018. Barite recrystallization in the presence of 226ra and 133ba. Geochimica et Cosmochimica Acta 232, 124–139.

Henisch, H., García-Ruiz, J., 1986. Crystal growth in gels and liesegang ring formation: Ii. crystallization criteria and successive precipitation. Journal of crystal growth 75, 203–211.

Kalo, K., Grgic, D., Auvray, C., Giraud, A., Drach, B., Sevostianov, I., 2017. Effective elastic moduli of a heterogeneous oolitic rock containing 3-d irregularly shaped pores. International Journal of Rock Mechanics and Mining Sciences 98, 20–32.

Klinkenberg, M., Brandt, F., Baeyens, B., Bosbach, D., Fernandes, M.M., 2021. Adsorption of barium and radium on montmorillonite: A comparative experimental and modelling study. Applied Geochemistry 135, 105117. URL: https://doi.org/10.1016/j.apgeochem.2021.105117, doi:10.1016/j.apgeochem.2021.105117.

Krumgalz, B.S., Pogorelsky, R., Sokolov, A., Pitzer, K.S., 2000. Volumetric ion interaction parameters for single-solute aqueous electrolyte solutions at various temperatures. Journal of Physical and Chemical Reference Data 29, 1123–1140.

Loon, L.R.V., Glaus, M.A., Frick, S., Bunic, P., Chen, Y., Wigger, C.,

Fukatsu, Y., Zhao, Y., 2016. DIFFUSION PROCESSES. Progress Report 2016. Paul Scherrer Institut.

Melkior, T., Gaucher, E.C., Brouard, C., Yahiaoui, S., Thoby, D., Clinard, C., Ferrage, E., Guyonnet, D., Tournassat, C., Coelho, D., 2009. Na+ and hto diffusion in compacted bentonite: Effect of surface chemistry and related texture. Journal of Hydrology 370, 9–20.

Millero, F.J., Ward, G.K., Chetirkin, P.V., 1977. Relative sound velocities of sea salts at 25 c. The Journal of the Acoustical Society of America 61, 1492–1498.

Miri, R., Hellevang, H., 2016. Salt precipitation during co2 storageâĂŤa review. International Journal of Greenhouse Gas Control 51, 136–147.

Morel, R., 1996. Les sols cultivés. Technique & documentation-Lavoisier.

Noiriel, C., Renard, F., Doan, M.L., Gratier, J.P., 2010. Intense fracturing and fracture sealing induced by mineral growth in porous rocks. Chemical Geology 269, 197–209.

Parkhurst, D.L., Appelo, C., et al., 2013. Description of input and examples for phreeqc version 3 – a computer program for speciation, batch-reaction, one-dimensional transport, and inverse geochemical calculations.

Poonoosamy, J., Curti, E., Kosakowski, G., Grolimund, D., Van Loon, L., Mäder, U., 2016. Barite precipitation following celestite dissolution in a porous medium: A sem/bse and μ-xrd/xrf study. Geochimica et Cosmochimica Acta 182, 131–144.

Poonoosamy, J., Klinkenberg, M., Deissmann, G., Brandt, F., Bosbach, D., Mäder, U., Kosakowski, G., 2020. Effects of solution supersaturation on barite precipitation in porous media and consequences on permeability: Experiments and modelling. Geochimica et cosmochimica acta 270, 43–60.

Poonoosamy, J., Kosakowski, G., Van Loon, L.R., Mäder, U., 2015. Dissolution–precipitation processes in tank experiments for testing numerical models for reactive transport calculations: Experiments and modelling. Journal of Contaminant Hydrology 177, 1–17.

Poupeleer, A.S., 2007. Transport and crystallization of dissolved salts in cracked porous building materials. Ph.D. thesis. KU Leuven.

Poupeleer, A.S., Roels, S., Carmeliet, J., Van Gemert, D., 2006. Diffusion-convection transport of salt solutions in cracked porous building materials part 1: Parameters, model description and application to cracks/transport von salzlösungen durch diffusion und konvektion in porösen werkstoffen des bauwesens mit rissen teil 1: Relevante parameter, beschreibung des modells und seine anwendung bei anwesenheit von rissen. Restoration of Buildings and Monuments 12, 187–204.

Prasianakis, N., Curti, E., Kosakowski, G., Poonoosamy, J., Churakov, S., 2017. Deciphering pore-level precipitation mechanisms. Scientific reports 7, 1–9.

Prieto, M., 2014. Nucleation and supersaturation in porous media (revisited). Mineralogical Magazine 78, 1437–1447.

Prieto, M., Putnis, A., Arribas, J., Fernandez-Diaz, L., 1992. Ontogeny of baryte crystals grown in a porous medium. Mineralogical Magazine 56, 587–598.

Prieto, M., Putnis, A., Fernandez-Diaz, L., 1990. Factors controlling the kinetics of crystallization: supersaturation evolution in a porous medium. application to barite crystallization. Geological Magazine 127, 485–495.

Puchalska, D., Atkinson, G., 1991. Densities and apparent molal volumes of aqueous bacl2 solutions from 15 to 140. degree. c and from 1 to 200 bar. Journal of Chemical and Engineering Data 36, 449–452.

Putnis, A., Mauthe, G., 2001. The effect of pore size on cementation in porous rocks. Geofluids 1, 37–41.

Putnis, A., Prieto, M., Fernandez-Diaz, L., 1995. Fluid supersaturation and crystallization in porous media. Geological Magazine 132, 1–13.

Radilla, G., Kacem, M., Lombard, J., Fourar, M., 2010. Transport properties of lavoux limestone at various stages of co2-like acid-rock alteration. Oil & Gas Science and Technology–Revue de lâĂŹInstitut Français du Pétrole 65, 557–563.

Rajyaguru, A., L'Hôpital, E., Savoye, S., Wittebroodt, C., Bildstein, O., Arnoux, P., Detilleux, V., Fatnassi, I., Gouze, P., Lagneau, V., 2019. Experimental characterization of coupled diffusion reaction mechanisms in low permeability chalk. Chemical Geology 503, 29–39.

Rajyaguru, A., Wang, J., Wittebroodt, C., Bildstein, O., Detilleux, V.,

Lagneau, V., Savoye, S., 2021. Barite precipitation in porous media: Impact of pore structure and surface charge on ionic diffusion. Journal of Contaminant Hydrology 242, 103–851.

Rimmelé, G., Barlet-Gouédard, V., Renard, F., 2010. Evolution of the petrophysical and mineralogical properties of two reservoir rocks under thermodynamic conditions relevant for co2 geological storage at 3 km depth. Oil & Gas Science and Technology–Revue de lâĂŹInstitut Français du Pétrole 65, 565–580.

Ruiz-Agudo, C., McDonogh, D., Avaro, J.T., Schupp, D.J., Gebauer, D., 2020. Capturing an amorphous baso4 intermediate precursor to barite. CrystEngComm 22, 1310–1313. URL: http://dx.doi.org/10.1039/C9CE01555H, doi:10.1039/C9CE01555H.

Scherer, G.W., 2004. Stress from crystallization of salt. Cement and concrete research 34, 1613–1624.

Steiger, M., 2005. Crystal growth in porous materialsâĂŤi: The crystallization pressure of large crystals. Journal of crystal growth 282, 455–469.

Van Noort, R., Wolterbeek, T.K., Drury, M.R., Kandianis, M.T., Spiers, C.J., 2017. The force of crystallization and fracture propagation during in-situ carbonation of peridotite. Minerals 7, 190.